ACADEMIC AURORA, 2026, Vol. 1, 71-92
A double-blind, Peer-reviewed, Open-Access Research Journal Indexed in NepJOL
©2026. The Author(s). Published by Research Management Cell (RMC)
Tri-Chandra Multiple Campus, Tribhuvan University, Nepal

ISSN: 3149-7527 (Print)
ISSN: 3149-7535 (Online)

Integrated Evaluation of Block Geometry and Blast-Induced Fragmentation in the Jointed Rock Mass: Empirical and Numerical Approach

Nishant Shrestha[1], Bindu Thapaliya[1], Krishna Kumar Shrestha[2,3], *Prem Bahadur Thapa[1]

[1]Department of Geology, Tri-Chandra Multiple Campus, Tribhuvan University, Kathmandu, Nepal
[2]Central Department of Geology, Tribhuvan University, Kirtipur, Kathmandu, Nepal
[3]Geological Investigation Department (GID), Nepal Electricity Authority, Kathmandu, Nepal

***Corresponding E-mail:** prem.thapa@trc.tu.edu.np

Received: 27 December 2025; Accepted: 8 July 2026

Abstract

Quantitative characterisation of muck pile shape and size analysis, along with the natural block geometry is crucial for cost optimisation in large tunnelling operations, especially in complex geological terrain such as the Nepal Himalaya. In this study, 15 controlled-blast rounds were analysed very closely, and the empirical block-volume estimation, image-based fragment analysis, Zingg and Sneed–Folk shape classification, and three-dimensional distinct-element numerical analysis methods were used to identify the behaviour of the muck pile as well as the natural block. From the field, 853 rock fragments were measured along three orthogonal axes to calculate fragment size and volume. For the distinct-element analysis, the measurement of joint spacing, orientation, and persistence are incorporated. The analysis demonstrated that natural rock blocks predominantly have cubic geometries. On the other hand, blast-induced fragments are dominated by bladed and elongated shapes, indicating the rock mass's strong anisotropy. The statistical validation results demonstrate the strong linear correlations between field-measured and image-based fragment volumes ($R^2 = 0.786$, RMSE = 0.056, $p < 0.001$), and the relationship between empirically estimated and DEM-based block volumes ($R^2 = 0.831$, RMSE = 0.07, $p < 0.001$) is more reliable, with a high R-square, Low RMSE, and p-value. The results reveal the strong relation between field observations, image-based analysis, numerical simulations, and empirical predictions, which confirms the applicability of the proposed integrated fragmentation framework for optimising tunnel blasting performance in the drill-and-blast tunnel.

Keywords: Rock mass, block geometry, blast fragmentation, empirical/numerical approach, Himalayan terrain.

Introduction

The shape and size characteristics of fragments, along with natural block geometry, play a critical role in tunnel excavation to optimise costs and ensure operational safety, especially in mountainous regions where heterogeneous, anisotropic rock masses exhibit distinct rock characteristics (Read and Stacey, 2010; Song et al., 2022). In the highly fragile rock of mountainous regions like Nepal, the transitional layering of bedrock with highly fractured rock and dense joint planes tends to be highly deformed, leading to distinct fragment shapes during tunnel blasting, which directly influences tunnel stability and muck pile excavation cycle-time productivity (Singh et al., 2016; Shrestha et al., 2023; Rahman et al., 2025). The impact of the bladed and elongated interlocked fragments on excavation efficiency in the case of load and unloading of muck piles, which consumes lots of time and effort. In contrast, equidimensional fragments enhance greater mobility, emphasising the crucial role of fragment morphology in optimising the time consumed (Kinyua et al., 2022; Kujundžić et al., 2021).

The numerical characterisation of fragment shape and size has been determined from sieve analyses to advanced photometric approaches. Various analysis methods, such as WipFrag, have enabled the prediction of particle-size distributions, including D_{10}, D_{50}, D_{90}, mean fragment size, uniformity index and characteristic size from the high-resolution images (Maerz et al., 1996; Guo et al., 2022). Besides, shape classification systems proposed by Zingg (1935), Sneed and Folk (1958) provide strong metrics of elongation, flatness and compactness of the shape of fragments, allowing for quantitative assessment of fragment interlocking potential, flowability and mechanical loading efficiency during the muck pile loading period (Kinyua et al., 2022). Apart from field-based analysis, advanced numerical modelling (DEM) offers a powerful framework for simulating natural block geometries derived from discontinuity sets, which results in realistic 3D block shape and size distributions along with anisotropy-controlled mechanisms. These DEM methods have been able to provide more reliable results over traditional analytical methods, including wedge analysis, limit-equilibrium block theory, and over-simplified empirical joint-spacing relations, which commonly overlook complex block interactions and three-dimensional kinematics (Aliabadian et al., 2014; Ghaedi et al., 2022; Jing and Hudson, 2002).

The empirical block volume estimation method based on Palmström's relation remains a strong foundation for predicting in-situ block sizes, which includes joint spacing and its orientation (Palmström, 2005; Koulibaly et al., 2023). However, the integrated analyses that combine the fragment-shape classification system, image-based size distribution, Palmström's empirical block-volume estimation, and numerical simulations from DEM across multiple blast rounds remain limited, particularly for structurally complex Himalayan terrains. Applying the integrated methods enhances the ability to predict the muck pile unloading capacity from the excavation site to enhance the efficiency, productivity, and tunnel face stability under highly fragile rock mass with distinct stress conditions in a reliable way (Ghaedi Ghalini et al., 2022; Kinyua et al., 2022; Zeng et al., 2025). Recent studies focus on rock mass deformation characteristics and support performance in the fragile Himalayan rock mass of different qualities (Thapaliya et al., 2025; Shrestha et al., 2026). Although fragmentation behaviour and natural block geometry are critical for blast efficiency and excavation control.

This study aims to introduce an integrated fragmentation analysis framework for the Nepal Himalaya that combines Zingg and Sneed–Folk fragment shape analysis, image-based particle size distribution, Palmström-derived block volume estimation, numerical simulation of natural block geometry from DEM and ellipsoidal average fragment volume calculations through the Palmström method. The data were collected in a systematic way from fifteen blast rounds. This analysis explicitly relates the pre-existing natural block structure and post-blast fragment morphology. The introduction of the structural framework to understand blast interactions with fragment shape and size provides insights for optimising blast design, improving muck-flow dynamics, and enhancing tunnelling efficiency within highly anisotropic and discontinuous rock masses.

Geology and Rock Mass Characteristics

The study area lies in the Higher Himalayan Crystalline Zone, north of the Main Central Thrust (MCT), and the area extends between latitudes 27°26′52″ to 27°30′29″N and longitudes 87°36′30″ to 87°38′15″E (**Figure 1**). The tunnel alignment traverses predominantly through foliated banded gneiss and feldspathic augen gneiss, with northward-dipping foliations. The discontinuities in the rock mass have dominant orientations of 355°/25°, 015°/30°, 030°/35° and 320°/40°. The rock mass quality along the tunnel alignment varies considerably, with rock mass rating (RMR) values ranging from 20 to 60, indicative of very poor to good rock mass quality. Similarly, Q-system values range from 0.1 to 4, which correspond to weakly to moderately jointed, blocky rock masses.

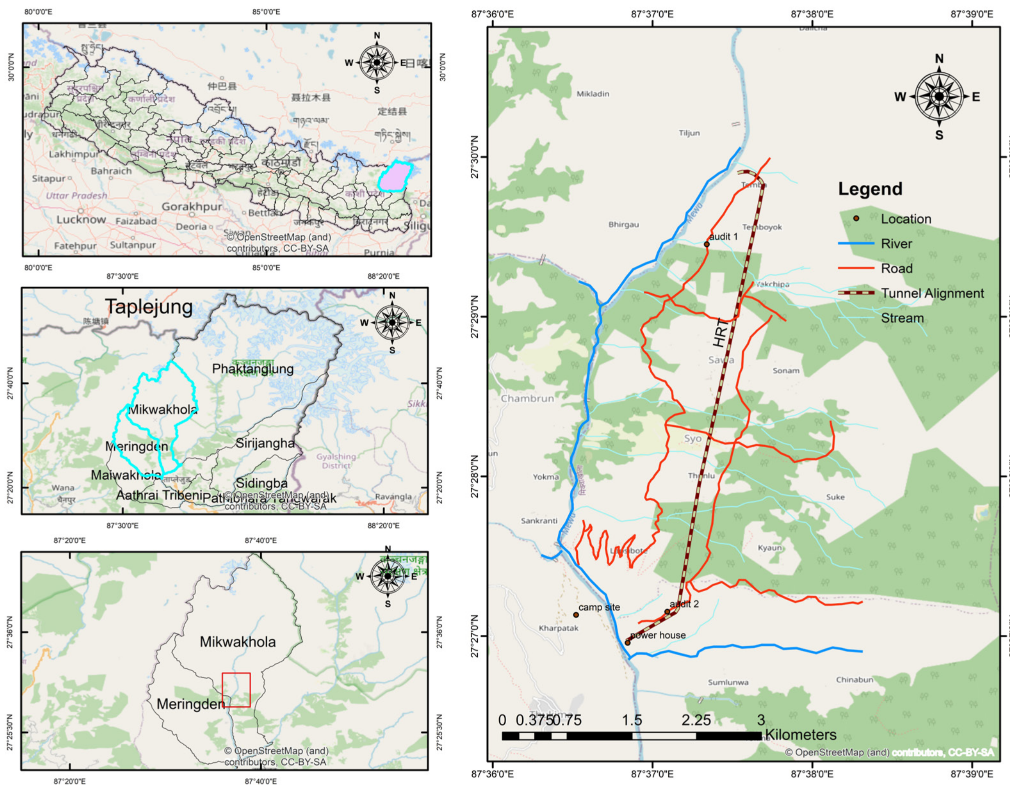

Figure 1: *Location map of study area.*

Methodology

Fragment morphology and block geometry were characterised through systematic field measurements and supported by image-based analyses, empirical approaches, and numerical modelling techniques (**Figure 2**).

Fragments Shape Analysis

A total of 853 rock fragments were collected from 15 controlled blast rounds, with more than 45 representative fragments measured from each blast. Each fragment was measured along three mutually orthogonal axes: the longest axis (*a*), intermediate axis (*b*) and the shortest axis (*c*). These geometric measurements form the basis for classification of fragment shape and volumetric assessment. To classify the shape of blast fragments, two classification systems developed by Zingg (1935) and Sneed and Folk (1958) are considered. The Zingg (1935) classification system uses dimensionless axis ratios R_1 = b/a and R_2 = c/b and categorises the fragments into four fundamental shape categories: blade, disc, rod and sphere. It enables identification of each fragment shape by its relative elongation and flatness. The Sneed and Folk

(1958) classification system categorizes the produced fragments into 10 shape classes where standard shape value ranges 0 to 1. The lower values indicate platy shape, intermediate values represent equant or cubical fragment shape and higher values correspond to elongated or bladed shape classes.

Photogrammetric Analysis of Rock Fragmentation

The high-resolution photographs of muck piles were analysed to determine the particle size distribution of blast-induced rock fragments. These images provide quantitative estimation of standard fragmentation size distribution parameters, D_{10}, D_{50}, D_{90}, mean fragment size, and the uniformity index $(N=D_{90}/D_{10})$. To analyse particle size distribution of blast fragments, five representative photographs of muck piles from each blast round were captured to minimise the possible measurement errors. These photographs were then processed via photogrammetric analysis to delineate particle boundaries and to identify particle size distribution. The representative fragment size distribution for each blast was obtained from the average measurements of five images processed through photogrammetric analysis.

Natural Block Volume Estimation (Empirical Method)

The natural block volumes were estimated using the empirical relation based on Palmström's block volume quantification technique. From the field investigation, three dominant joint sets were identified: J_1 (280°–355°/35°–45°), J_2 (130°–141°/38–70°), and J_3 (260°–290°/30–62°). The joint spacings range from 0.23 to 0.42 m for set J_1 (S_1), 0.446 to 0.58 m for set J_2 (S_2) and 0.60 to 0.72 m for set J_3 (S_3). The orientation of joints in the rock mass determines the angles between intersecting joint sets required for block volume estimation. The natural block volume (V_b) was calculated using Eq. 1:

$$V_b = \frac{1}{6}\, S_1 .\, S_2 .\, S_3 \,\sin\gamma_1 \,.\, \sin\gamma_2 .\, \sin\gamma_3 \qquad (1)$$

where, S_1, S_2, and S_3 are the mean spacings of the three dominant joint sets (m)

$\gamma_1, \gamma_2, \gamma_3$ are the angle between the respective intersecting joint planes.

This equation provides a practical estimate of in situ block size thereby explicitly accounting the influence of joint spacing and joint set geometry.

Numerical Block Volume Simulation

Along with the empirical method, the block volumes were assessed from three-dimensional numerical simulations using the distinct element method (DEM). The DEM explicitly models block formation in a jointed rock mass by incorporating discrete discontinuity characteristics. The input parameters include the number of joint sets, dip and dip direction, spacing, and persistence of discontinuity. The dominant joint sets are J_1 (280–355°/35–45°), J_2 (130–141°/38–70°), and J_3 (260–290°/30–

62°) with joint persistence exceeding 3 m. The spacing for these joint set ranges from 0.23 to 0.42 m for s_1, 0.446 to 0.58 m for s_2, and 0.60 to 0.72 m for s_3. Integration of these parameters in the model generate discrete block geometry representative of in situ structural conditions.

The numerical model configuration presents a tunnel face with dimensions of 3.92 m (width), 4.28 m (height), and 2.50 m (average pull length), corresponding to a single blast round. Model generation and analysis were performed using standard DEM commands including new, poly brick, plot block colour by mat, and print max to define the block domain, assign joint properties and extract block volume statistics. Simulations were performed at the tunnel face, and a total of 15 blast rounds were numerically modelled. For each simulation, the minimum, average and maximum block volumes were obtained directly from the numerical output.

Fragment Shape and Volume Calculation (Ellipsoidal Method)

Average fragment volumes were calculated from measured fragment dimensions using an ellipsoidal volume equation (Eq. 2) (Bronshtein et al., 2015):

$$V_f = \frac{4}{3}\pi\left(\frac{a}{2}\right)\left(\frac{b}{2}\right)\left(\frac{c}{2}\right) \quad (2)$$

where, a, b, and c represent the three orthogonal axes of the individual fragment. The dimensions measured in the field were used to provide a consistent geometric representation for quantifying the volume of blast-induced fragments.

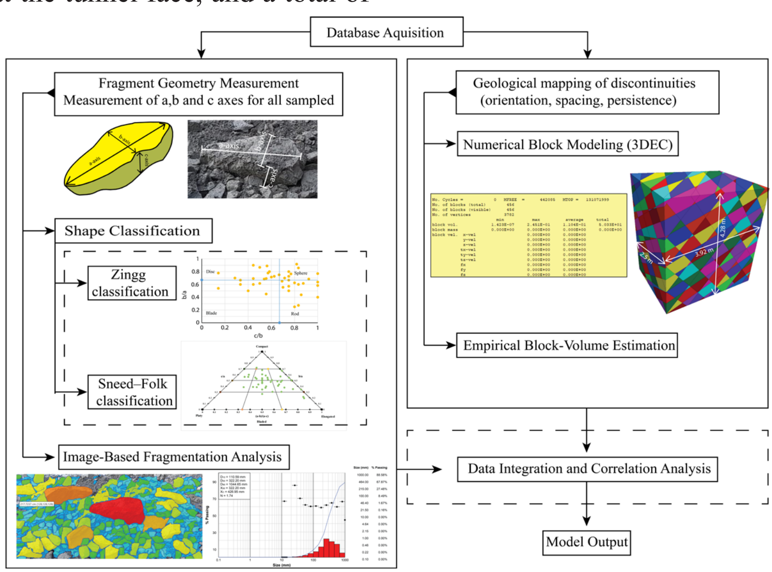

Figure 2: *Integrated workflow for quantifying the shape and size of rock fragments and natural blocks.*

Results

The results are described in terms of fragment shape characterisation and natural block volume estimation. Shape variability of blasted rock mass was elaborated in terms of a classification system and analytical approach.

Fragment Shape Characterisation

Zingg Classification System

The fragment geometry was analysed using the Zingg classification system for a total of 853 fragments collected from 15 blast rounds. The overall dataset indicates that blade-shaped fragments constitute the most significant proportion (38.9%), followed by disc-shaped (25.1%), rod-shaped (24.1%) and sphere-shaped fragments (12.0%) (**Figure 3**).

The blade-shaped fragments are dominant, with a range between 22.92 and 52.63%; disc-shaped fragments from 17.31% to 31.31%; rod-shaped fragments from 15.79% to 33.33%; and sphere fragments from 4.17% to 17.80% (**Table 1**). The proportion of rock fragment shape for each blast round is presented in **Figure 4**. The prevalence of blade and disc-shaped fragments in each blast reflects the strong structural anisotropy of schistose gneiss. The closely spaced discontinuities and foliation of schistose gneiss have controlled the development of elongated and platy fragments during blasting.

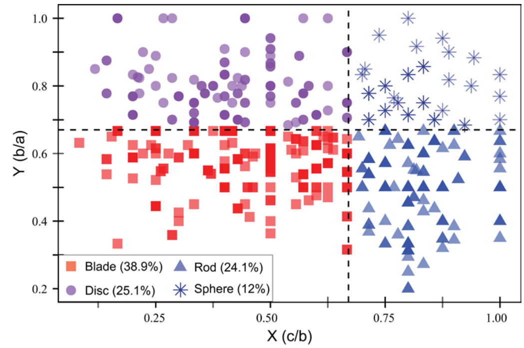

Figure 3: *Overall Zingg shape classification of fragments.*

Table 1: *Distribution of rock fragment shapes.*

Blast No.	Zing classification for shape (%)			
	Blade	Dis	Rod	Sphere
1	17.8	31.1	33.3	17.8
2	37.5	31.25	25	6.25
3	32.65	28.57	30.61	8.16
4	43.75	31.25	20.83	4.17
5	52.63	17.54	15.79	14.04
6	22.92	29.17	33.33	14.58
7	42.62	22.95	19.67	14.75
8	42.62	26.23	22.95	8.2
9	36.07	27.87	21.31	14.75
10	34.43	26.23	27.87	11.48
11	42.62	22.95	19.67	14.75
12	40.98	22.95	26.23	9.84
13	42.62	21.31	24.59	11.48
14	44.26	21.31	21.31	13.11
15	40.98	21.31	22.95	14.75

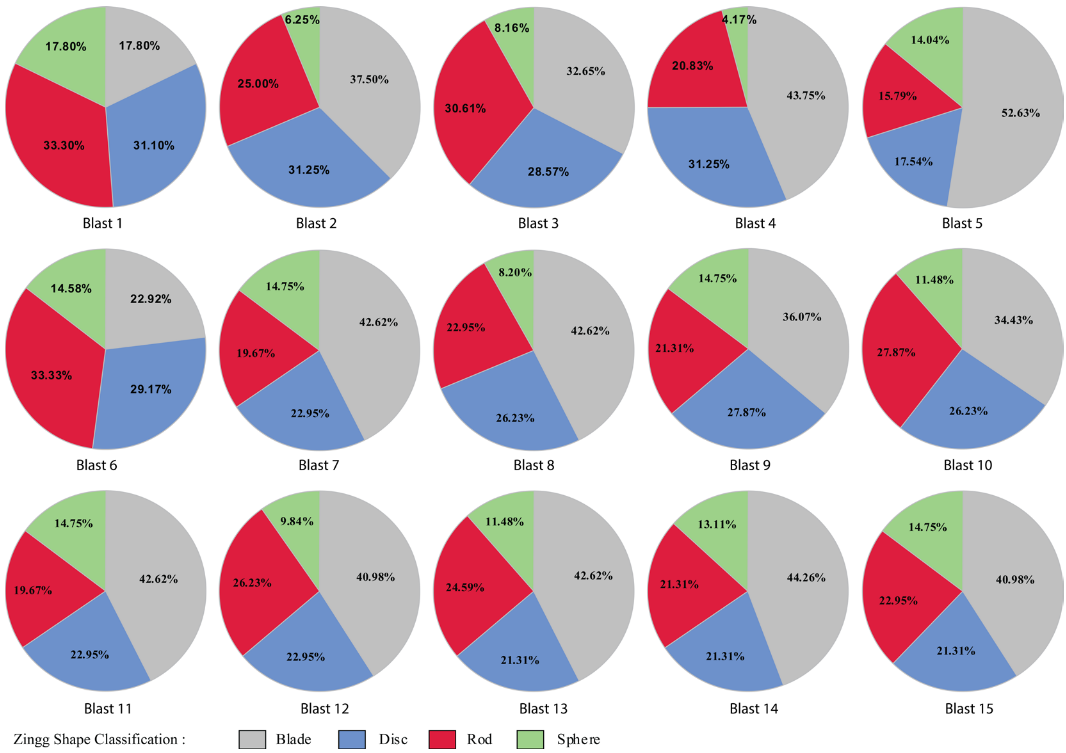

Figure 4: *Proportion of rock fragment shapes based on Zingg classification.*

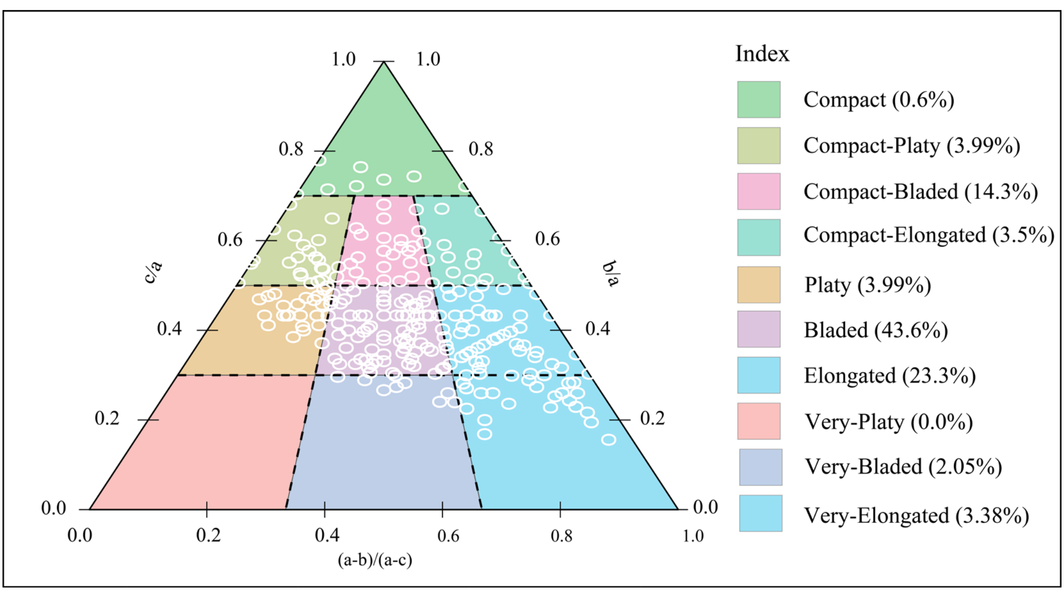

Figure 5: *Overall Sneed and Folk (1958) shape classification for fragments analysis.*

Table 2: *Distribution of blasted rock fragment shapes.*

Blast No.	Sneed and Folk classification									
	Compact	Compact platy	Compact bladed	Compact elongated	Platy	Bladed	Elongated	Very platy	Very blade	Very elongated
1	2.4	7.3	24.3	9.7	2.4	26.8	19.5	-	2.4	4.8
2	-	8.3	12.5	-	12.5	29.5	16.6	-	-	10.4
3	4.3	6.5	6.5	6.5	10.8	23.9	26.0	-	6.5	8.7
4	2.2	6.8	4.5	4.5	13.6	31.8	22.7	-	2.2	11.3
5	5.7	3.8	5.7	3.8	3.8	42.3	23.0	-	5.7	5.7
6	-	11.1	15.5	8.8	11.1	20	24.4	-	-	8.8
7	-	7.8	13.7	3.9	7.8	41.1	17.6	-	3.9	3.9
8	-	7.8	13.7	3.9	7.8	41.1	17.6	-	3.9	3.9
9	-	7.3	12.9	3.7	7.3	42.6	16.6	-	5.5	3.7
10	-	8.3	8.3	8.3	4.1	45.8	18.7	-	2.0	4.1
11	-	7.8	7.8	7.8	3.9	43.1	23.5	-	1.9	3.9
12	-	7.84	11.76	3.92	7.84	47.06	15.69	-	1.96	3.92
13	-	7.4	14.8	3.7	3.7	46.3	16.6	-	1.8	5.5
14	-	4.0	14.2	4.0	8.1	46.9	16.3	-	2.0	4.0
15	-	7.5	13.2	3.7	3.7	47.1	18.8	-	1.8	7.5

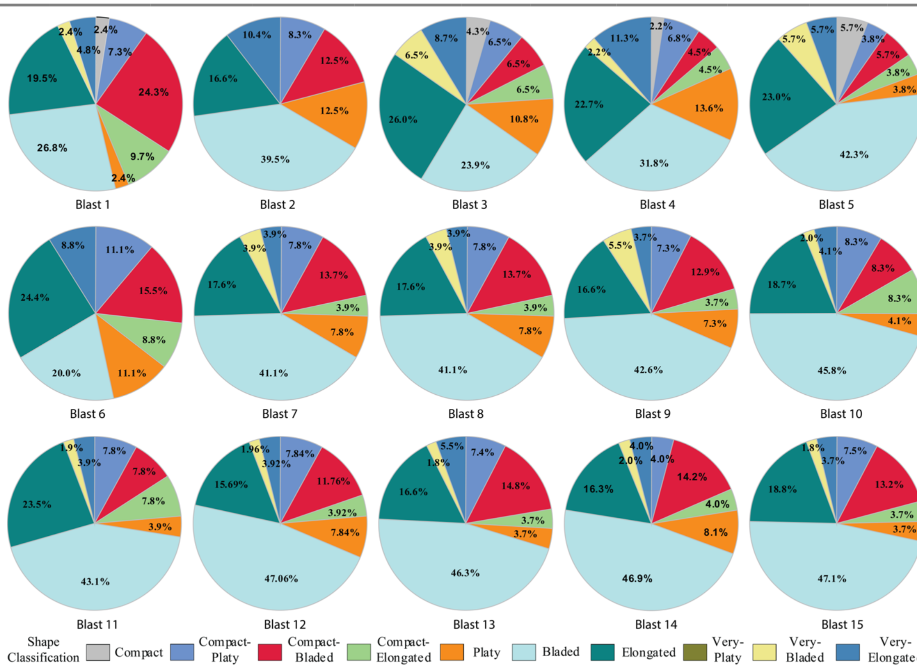

Figure 6: *Plots of rock fragment shapes based on Sneed and Folk classification.*

Sneed and Folk's (1958) classification

The Sneed and Folk shape classification was used to characterise the three-dimensional morphology of rock fragments. The results show a strong dominance of anisotropic fragment forms (**Figure 5**). Bladed fragments account for 43.6%, followed by elongated fragments (23.3%). Subordinate shape classes include compact bladed (14.3%), compact platy (3.99%) and platy fragments (7.8%), whereas compact elongated fragments represent only 3.99%. Extremely anisotropic forms occur only in minor proportions, with very elongated (3.38%) and very bladed (2.05%) fragments together accounting for less than 5.5% of the dataset. Notably, compact equidimensional (0.6%) and very platy fragments are absent (0%), indicating that sphere fragmentation is insignificant within the blasted rock mass.

Evaluation of each blast round revealed a consistent predominance of bladed and elongated fragment shapes, despite moderate variability being evident between individual blast rounds (**Figure 6**, **Table 2**). During these blast rounds, elongated fragments consistently accounted for 19.0–28.6%, underscoring the prevalence of non-equidimensional shapes. The analysis identified that compact bladed fragments typically varied from 9.5% to 19.0%, whereas compact platy and compact elongated shapes rarely exceeded 10% individually. Very bladed and very elongated fragments appeared sporadically and typically remained below 7%. The shape classification shows a predominance of bladed and elongated morphologies. The analysis revealed strong structural control of discontinuities and the inherent rock anisotropy indicating the preferential direction of splitting during blasting operations.

Image-based fragment size distribution analysis

A blast-wise particle size distribution analysis was conducted using photogrammetric analysis to evaluate blast fragmentation rock mass characteristics and blasting design efficiency (**Figure 7**). The analysis of fragmentation characteristics across the 15 blast rounds is shown in **Table 3**. Blast 1 is characterised by relatively coarse fragmentation, with D_{10} = 106.5 mm, D_{50} = 301.4 mm and D_{90} = 1035.1 mm. The corresponding fragment size (X_{50}) of 406.2 mm in this blast indicates limited breakage and the formation of oversized blocks. In contrast, blast 2 produced a significant amount of finer fragmentation (D_{10} = 24.6 mm, D_{50} = 77.1 mm, D_{90} = 260.7 mm), with a substantially lower X_{50} of 108.9 mm, indicating a more efficient energy distribution and corresponding improved breakage. A similar fine fragmentation pattern is observed in Blast 3, where D_{50} decreased to 70.2 mm and X_{50} to 98.9 mm. The presence of large fragments (PAR = 4788 mm) in blast fragments revealed the high control of structural geology, such as dense joints and fractures within the rock mass. Blast 4 exhibited moderate fragmentation, with D_{50} = 96.7 mm and X_{50} = 130.7 mm, which lies between the coarser and finer blast outcomes.

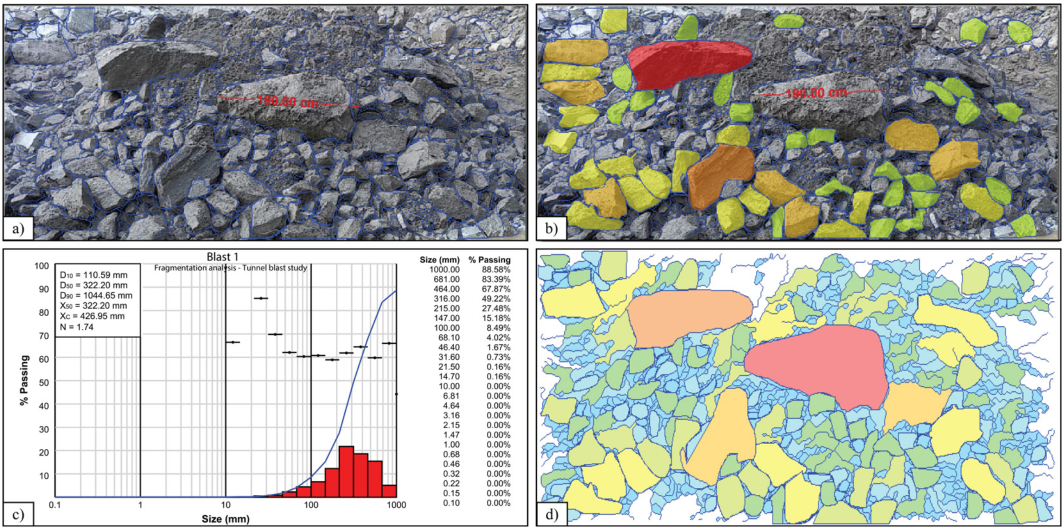

Figure 7: *Image-based analysis of muck pile deposits (a) muck pile from excavation, (b) fragment size analysis, (c & d) output results.*

Table 3: *Parametric evaluation of photogrammetric-based analysis of blast fragments.*

Parameter → Blast No.↓	D_{10}	D_{50}	D_{90}	Mean Fragment Size (X_{50})	Uniformity index (N)	Characteristics size (Xc)
1	106.5	301.4	1035.1	1.7	406.2	1296.0
2	24.6	77.1	260.7	1.5	108.9	4740.0
3	24.7	70.2	297.9	1.7	98.9	4788.0
4	37.5	96.7	302.8	1.7	130.7	4757.0
5	16.7	38.0	90.1	2.0	45.9	12226.0
6	63.4	181.1	523.3	1.7	237.4	12151.0
7	93.1	237.5	733.5	1.9	301.5	4961.0
8	56.4	344.5	855.7	344.5	1.4	445.7
9	36.0	193.7	410.9	193.7	1.4	268.3
10	30.0	69.1	174.7	69.1	2.1	90.3
11	13.6	63.4	220.6	63.4	1.3	94.6
12	36.4	193.7	410.9	193.7	1.4	268.3
13	44.7	210.4	728.9	210.4	1.2	471.1
14	30.8	135.2	259.9	135.2	1.8	164.3
15	107.5	301.4	1035.1	301.4	1.7	406.2

The smallest fragmentation was observed in Blast 5, with D_{10} = 16.7 mm, D_{50} = 38.0 mm, and D_{90} = 90.1 mm, indicating a small mean fragment size (X_{50}) of 45.9 mm with highly efficient in breakage. Blast 6 shows a shift toward coarser fragmentation (D_{50} = 181.1 mm, X_{50} = 237.4 mm), which becomes further pronounced in Blast 7 (D_{50} = 237.5 mm, X_{50} = 301.5 mm). Blast 8 exhibits one of the coarsest particle size distributions, with D_{50} = 344.5 mm, D_{90} = 855.7 mm, and Xc = 445.7 mm, suggesting dominant block release along persistent discontinuities. The intermediate fragmentation is observed in Blast 9 (D_{50} = 193.7 mm, X_{50} = 268.3 mm), whereas blasts 10 and 11 again show relatively fine fragmentation, with D_{50} values of 69.1 mm and 63.4 mm, respectively. Blast 12 shows fragmented characteristics similar to Blast 9. Blast 13 produces coarser fragments (D_{50} = 210.4 mm, D_{90} = 728.9 mm, Xc = 471.1 mm), followed by blast 14 which shows moderate fragmentation (D_{50} = 135.2 mm, X_{50} = 164.3 mm). Finally, Blast 15 yields one of the coarsest fragmentation outcomes, closely resembling blast 1 with D_{50} = 301.4 mm, D_{90} = 1035.1 mm and X_{50} = 406.2 mm, indicating substantial oversize of muck. The results of fragmentation efficiency are mainly influenced by rock mass heterogeneity, the persistence and orientation of discontinuity and local variations in burden–spacing geometry and explosive energy distribution under nominally similar blast designs.

Natural Block Volume Estimation

The natural block volume is calculated based on empirical approaches, shape analysis, and block size measurements. The results are further validated by statistical methodologies.

Empirical estimation of natural block volume

The approach enables a realistic estimation of in situ block geometry before blasting by incorporating both discontinuities spacing and their orientation. From the field, joint spacing for all three planes remains within relatively narrow ranges (S_1 = 0.23–0.43 m, S_2 = 0.446–0.58 m, S_3 = 0.60–0.72 m), whereas the intersection angles between these three planes show considerable variability, which strongly influences the calculated block volumes (**Table 4**).

For Blast 1, the discontinuity spacing is combined with high intersection angles (γ_1 = 67°, γ_2 = 22°, γ_3 = 87°), resulting in 0.374 m^3 (natural block volume). Blast 2 has one of the smallest block volumes (0.138 m^3) despite the presence of comparable spacing, as the very high intersection angles (γ_1–γ_3 = 75–81°) favour finer natural block subdivision. In contrast, Blast 3 shows an increase in block volume to 0.392 m^3, which is caused by wider spacing along S_3 (0.70 m) and high sine values for γ_1 and γ_3. Blast 4 yields a moderate block volume (0.244 m^3), though S_3 spacing is relatively wide (0.72 m). The smaller γ_2 angle restricts block enlargement and reduces overall block volume.

Table 4: *Calculated natural block volumes based on empirical methods.*

Blast No.	S_1	S_2	S_3	J_1	J_2	J_3	γ_1	γ_2	γ_3	$\sin\gamma_1$	$\sin\gamma_2$	$\sin\gamma_3$	Block Vol. (m^3)
1	0.39	0.55	0.6	40/280	38/140	62/275	67	22	87	0.921	0.375	0.999	0.374
2	0.33	0.58	0.67	39/359	70/140	55/260	81	75	78	0.988	0.964	0.978	0.138
3	0.4	0.58	0.7	45/290	40/135	55/260	83	25	83	0.992	0.421	0.992	0.392
4	0.38	0.58	0.72	35/355	60/130	30/275	88	41	86	1.000	0.652	0.997	0.244
5	0.39	0.51	0.68	35/330	50/140	35/280	87	28	81	0.998	0.476	0.987	0.288
6	0.33	0.57	0.62	43/350	30/140	30/290	71	38	58	0.948	0.613	0.846	0.237
7	0.43	0.53	0.64	35/325	60/130	51/290	85	29	72	0.996	0.480	0.950	0.321
8	0.23	0.515	0.625	40/295	38/141	55/276	50	52	35	0.766	0.78801	0.5736	0.21382
9	0.293	0.485	0.625	39/358	70/141	60/265	51	20	30	0.7771	0.34202	0.866	0.37076
10	0.412	0.446	0.645	45/300	40/136	57/262	45	50	33	0.7071	0.76604	0.8387	0.53841
11	0.42	0.483	0.665	45/340	60/131	30/276	45	30	60	0.7071	0.5	0.5	0.96834
12	0.293	0.512	0.635	35/320	50/141	40/281	55	40	50	0.8192	0.64279	0.766	0.42822
13	0.32	0.463	0.63	43/350	30/141	35/285	47	60	55	0.7314	0.5	0.8192	0.4394
14	0.42	0.492	0.625	40/325	60/131	53/281	50	30	37	0.766	0.5	0.6018	0.56028
15	0.43	0.53	0.715	42/281	38/142	60/269	48	52	30	0.7431	0.78801	0.5	0.55651

Blast 5 has a natural block volume of 0.288 m^3, resulting from wide spacing and intersection angles, while blast 6 has a smaller volume of 0.237 m^3 due to reduced angular intersections (particularly γ_3), which reduces the effective block size. An increment of block volume in blast 7 to 0.321 m^3 is due to wider S_1 spacing (0.43 m) and favourable joint orientation. Blast 8 produced a comparatively lower block volume (0.214 m^3). This reduction in block dimension, even in closely spaced joints, is primarily controlled by smaller intersection angles (γ_1–γ_3 = 35–52°).

Larger natural block volumes were calculated for blasts 9 and 10, yielding volumes of 0.371 m^3 and 0.538 m^3 respectively. The higher volume in blast 10 is influenced by lower intersection angles, which increased block size. Blast 11 has combined effects of wide joint spacing and relatively low values of intersection angles, which resulted the largest estimated block volume (0.968 m^3). Blasts 12 and 13 yielded similar block volumes of 0.428 m^3 and 0.439 m^3, respectively. Blast 14 also produced a large block volume (0.560 m^3), aligning with reduced γ_2 and γ_3 values, while blast 15 yielded a comparable estimate (0.557 m^3) under similar structural conditions.

Overall joint orientation and intersection angles control block volume more strongly than spacing alone. The natural block volumes range from 0.138 m^3 to 0.968 m^3 with a significant variability in natural block size. The results indicate that joint orientation and intersection angles control block volume more strongly than spacing alone. Smaller intersection angles (i.e., lower $\sin\gamma$ values) lead to markedly larger computed block volumes, even where joint spacing is broadly comparable.

Numerical estimation of natural block volume

A three-dimensional discontinuum analysis was conducted to evaluate blast-wise block generation and the resulting block volume distribution by explicitly incorporating joint set geometry and spacing (**Figure 8**). The three orthogonal spacing parameters (S_1–S_3) with the orientations of three dominant joint sets (J_1–J_3) which enables a realistic simulation of block formation within the rock mass is incorporated to calibrate the model. The measured spacing values for S_1 range from 0.23 to 0.43 m, S_2 from 0.446 to 0.58 m, and S_3 from 0.60 to 0.72 m. This spacing indicates heterogeneous structural conditions along the blast face across the fifteen blast rounds (**Table 5**).

Joint spacings of S_1 = 0.39 m, S_2 = 0.55 m, and S_3 = 0.60 m, combined with joint orientations of J_1 = 40/280°, J_2 = 38/140°, and J_3 = 62/275°, for blast 1 resulted in a wide block volume range, with volumes varying from 2.2×10^{-7} m^3 to 0.9294 m^3 and an average block volume of 0.1989 m^3. A tight spacing (S_1 = 0.33 m) with steep joint orientations in Blast 2 generated smaller blocks with a reduction in maximum volume of 0.1601 m^3 and a lower average volume of 0.0751 m^3. In Blast 3, increased S_3 spacing (0.70 m) led to a higher maximum block volume of 0.3898 m^3, even though the minimum block volume remains very small (1.7×10^{-6} m^3).

In Blast 4, wider joint spacing S_3 (0.72 m) and unfavourable joint intersections yielded block volumes ranging from 1.4×10^{-7} m^3 to 0.2451 m^3, with an average of 0.1104 m^3. Blast 5 generated a uniform block with an average volume of 0.1237 m^3, attributed to spacing values for S_1 = 0.39 m, S_2 = 0.51 m, and S_3 = 0.68 m. Blast 6 produced one of the widest volume distributions. The maximum block volume is 0.9586 m^3, and the average block size is 0.1291 m^3.

Blasts 7 to 10 have comparable joint spacing and orientation, generating intermediate block volumes. Both blasts 8 and 10 showed the maximum volume during simulation at 0.93 m^3 and 0.39 m^3, respectively; however, Blast 7 has an average volume of 0.126 m^3 due to the major role of the persistent joint. Similarly, in Blast 9, due to closer spacing along S_1 and S_2, it revealed the smallest average volume of 0.0751 m^3.

Table 5: *Calculated natural block volumes using numerical methods for blast rounds.*

Blast No.	S_1	S_2	S_3	J_1	J_2	J_3	Min	Max	Average	Total (m^3)
1	0.39	0.55	0.6	40/280	38/140	62/275	2.2E-07	0.9294	0.1989	
2	0.33	0.58	0.67	39/355	70/140	55/260	4.9E-07	0.1601	0.07513	
3	0.4	0.58	0.7	45/290	40/135	55/260	1.7E-06	0.3898	0.1434	
4	0.38	0.58	0.72	35/355	60/130	30/275	1.4E-07	0.2451	0.1104	
5	0.39	0.51	0.68	35/330	50/140	35/280	3.5E-07	0.4156	0.1237	
6	0.33	0.57	0.62	43/350	30/140	30/290	2.4E-07	0.9586	0.1291	
7	0.43	0.53	0.64	35/325	60/130	51/290	3.3E-07	0.3675	0.126	
8	0.23	0.515	0.625	40/295	38/141	55/276	2.2E-07	0.9294	0.1989	50.33
9	0.293	0.485	0.625	39/355	70/141	60/265	4.9E-07	0.1601	0.07513	
10	0.412	0.446	0.645	45/300	40/136	57/262	1.7E-06	0.3898	0.1434	
11	0.42	0.483	0.665	45/340	60/131	30/276	1.4E-07	0.2451	0.1104	
12	0.293	0.512	0.635	35/320	50/141	40/281	3.5E-07	0.4156	0.1237	
13	0.32	0.463	0.63	43/350	30/141	35/285	2.4E-07	0.9586	0.1291	
14	0.42	0.492	0.625	40/325	60/131	53/281	3.3E-07	0.3675	0.126	
15	0.43	0.53	0.715	42/281	38/142	60/269	2.2E-07	0.9294	0.1989	

The distribution of block volume appears consistent with average volumes ranging from 0.1104 m^3 to 0.1989 m^3 for blasts 11–15. In contrast, blasts 13 and 15 showed maximum volumes of ~0.96 m^3 and ~0.93 m^3 due to local geological conditions and blasting efficiency, favourable to the formation of large blocks despite relatively similar spacing parameters. The total modelled volume remains constant at 50.33 m^3 for all blast rounds, allowing direct comparison of block size distributions between blast rounds.

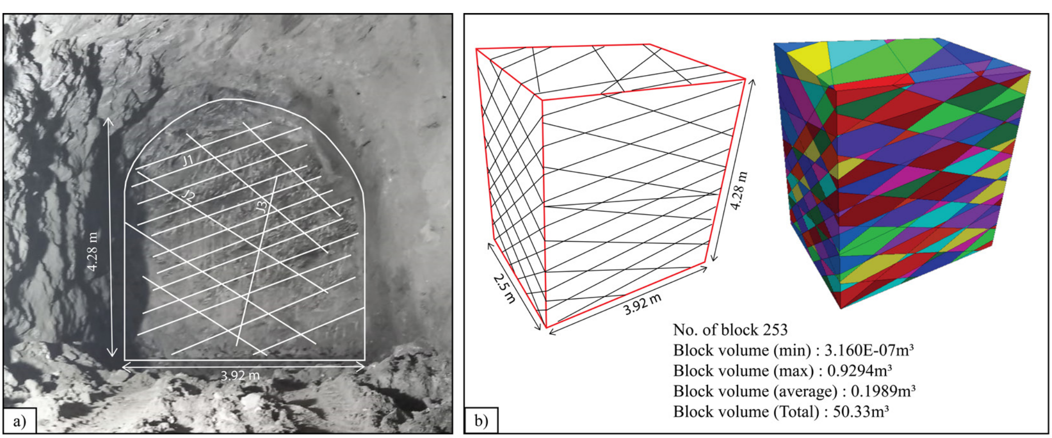

Figure 8: *Numerical estimation of natural block volume (a) tunnel face mapping, (b) block dimension analysis.*

Natural block shape analysis

The shape of natural rock blocks was characterized using the dimensionless shape ratios proposed by Palmström (2005). The three principal block dimensions (spacings) were arranged in ascending order as $S_1 \leq S_2 \leq S_3$, where S_1, S_2, and S_3 represent the shortest, intermediate, and longest block dimensions, respectively. The shape ratios were calculated as (Eq.3–4):

$$\alpha_2 = \frac{S2}{S1} \quad (3)$$

$$\alpha_3 = \frac{S3}{S1} \quad (4)$$

where, α_2 represents the ratio of the intermediate dimension to the shortest dimension, indicating the degree of block elongation, while α_3 represents the ratio of the longest dimension to the shortest dimension, reflecting the overall block aspect ratio or flatness. Values of α2 and α3 close to unity indicate nearly equidimensional (cubical) blocks, whereas higher values indicate increasingly elongated or platy block geometries.

Table 6: *Shape factors to estimate natural block for blast rounds.*

Blast No.	S_1	S_2	S_3	α_2	α_3	value	Shape
1	39.0	55.5	60.0	1.423077	1.538462	14.11622	Cubical block shapes of blasts
2	33.0	58.0	67.0	1.757576	2.030303	12.36902	
3	40.0	56.0	69.5	1.400000	1.73750	13.73895	
4	38.0	52.5	72.0	1.381579	1.894737	13.50952	
5	39.0	51.0	68.2	1.307692	1.748718	14.01932	
6	33.0	57.5	62.0	1.742424	1.878788	12.63703	
7	43.0	53.0	64.0	1.232558	1.488372	14.89917	
8	23.0	51.5	62.5	2.239130	2.717391	10.88761	
9	29.3	48.5	62.5	1.655290	2.133106	12.43754	
10	41.2	44.6	64.5	1.082524	1.565534	15.37516	
11	42.0	48.3	66.5	1.150000	1.583333	15.00686	
12	29.3	51.2	63.5	1.747440	2.167235	12.20210	
13	32.0	46.3	63.0	1.446875	1.968750	13.19449	
14	42.0	49.2	62.5	1.171429	1.488095	15.15395	
15	43.0	53.0	71.5	1.232558	1.662791	14.47632	

For the fifteen blast rounds, the calculated α_2 values ranged from 1.08 to 2.24, α_3 from 1.48 to 2.72. The resulting shape factors ranged between 10.88 and 15.38, where all fragments fall within the cubical category (**Table 6**).

Average fragment volume estimation based on block size

Table 7 presents the average volume from the total fifteen blast rounds, where Blast 1 has an average fragment volume of 0.0005 m^3, while Blast 2 indicated a higher value of 0.02198 m^3, due to the influence of joint spacing, rock mass characteristics, and blast energy distribution. Smaller average fragment volumes were observed in blasts 7, 11, 14, and 15 (0.00017–0.000171 m^3), indicating finer fragmentation, whereas Blast 8 generated relatively larger fragments (0.01554 m^3).

Table 7: *Average fragment and block volume estimation based on Palmström-derived block sizes.*

Blast No.	1	2	3	4	5	6	7	8	9	10	11	12	13	14	15
Ave. vol. cal. (10^{-3}×m^3)	0.5	2.2	0.4	0.5	2.9	0.4	0.2	1.5	0.3	0.2	0.2	0.3	0.6	0.2	0.2

Discussion

The comparison of natural block geometry and blast-induced fragment shapes provided valuable insights into the mechanisms and processes governing block volume formation and fragmentation. Both the empirical method and numerical analysis indicated that natural blocks exhibit a near-cubical geometry. Such block geometry is primarily controlled by in-situ joint spacing, orientation, and discontinuity persistence, which collectively define the rock mass's inherent block structure prior to blasting (Palmström, 2005). In contrast, Zingg and Sneed–Folk classifications of the fragment shape reveal a prevalence of bladed and elongated fragments and indicate strong anisotropy during fragmentation. The discrepancies are because of blasting, which leads to preferential splitting and separation along these discontinuities rather than along orthogonal block boundaries, resulting in structural weaknesses in foliation, schistosity, and joint planes. Similarly, Sanchidrián et al. (2017) and Johansson and Ouchterlony (2013) highlighted that the dominance of fragment shape and size is controlled by foliation and jointed rock mass. During explosive loading, stress directional release occurs from the jointed section. Analysis showed that bladed shape fragments are predominant across the sequential breakage, whereas shapes are absent in equidimensional fragments throughout the process. The natural block shape in the whole rock mass is equidimensional. As the results showed, the natural block shape is mostly dependent on characteristics of rock discontinuities (joints, fractures), the effects of drilling pattern and explosive energy also play a crucial role in blast fragments.

The image-based on average fragment volume show a strong and statistically significant linear correlation with the field measured average fragment volume (**Figure 9**). The observed regression equation $Y = 0.112X - 0.011$, with a coefficient of determination (R^2) of 0.786, indicates that the variance in field-measured volumes and image-based estimates is closely related (about 79%), demonstrating strong predictive consistency across the blast rounds. The low error metrics, such as RMSE = 0.056, MAE = 0.036, and MSE =

0.003, confirm the close relation in all blast rounds. In contrast, the very low p-value ($p = 1.07 \times 10^{-5}$) confirms that the observed correlation is statistically significant. Minor discrepancies are attributed to inherent limitations of two-dimensional image analysis, such as particle overlap, fines loss and scale calibration, compared with direct field measurements. Comparable levels of agreement between image-based fragmentation analysis and measured fragment volumes with $R^2 \approx 0.60–0.85$ have been reported in previous studies that have supported the reliability of image-based approaches as reliable and efficient tools for rapid fragmentation assessment (Maerz and Zhou, 1999; Johansson and Ouchterlony, 2013; Sanchidrián et al., 2017). Validation of methodology confirms that image-based fragmentation analysis provides a robust and statistically significant basis for estimating mean fragment volume in blasted rock masses.

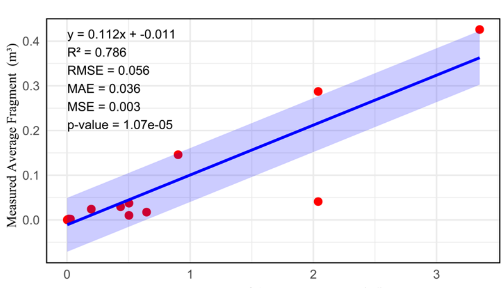

Figure 9: *Volumetric correlation of fragments between image-based analysis and measured values.*

The empirically estimated average block volume shows a strong and statistically significant linear relationship with the DEM-derived average block volume (**Figure 10**), which yielded the regression equation of $Y = 0.799X - 0.037$ with the coefficient of determination of $R^2 = 0.831$.The given level of relation is consistent in highly foliated schistose gneiss. The low error measures (RMSE = 0.07, MAE = 0.062, MSE = 0.005) show little scatter between the empirical and numerical approaches and suggest more stable predictive performance across all blast rounds. The very low p-value ($p = 2.23 \times 10^{-6}$) confirms that the observed relationship is statistically significant and unlikely to be due to random variation. Minor discrepancies are attributed to the simplifying assumptions inherent in empirical block volume formulations, which idealize block geometry, whereas the DEM approach explicitly accounts for joint persistence, block interaction and three-dimensional boundary constraints. The validation of the empirical approach provides a reliable estimate of natural block volume as a first-order solution whereas DEM-based numerical modelling is a more advanced method than others due to its refined, detailed and precise structural representation.

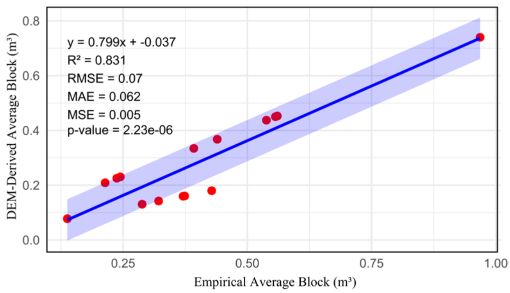

Figure 10: *Volumetric correlation between empirical average block analysis and numerically derived values.*

A comparative evaluation of average fragment volumes measured from field, image-based analysis, DEM model simulations, and empirical methods for volume calculation across fifteen blasts is presented in **Figure 11**. The measured fragment volumes in the field were consistently observed to be lower with little discrepancy, where Sanchidrián et al. (2014) and Ouchterlony and Sanchidrián (2019) also reported similar patterns in their studies. Conversely, the image-based analysis estimates exhibit little fluctuation and occasional extreme peaks, indicating an overestimation of rock fragment volume due to 2D image constraints and scale uncertainty as noted in earlier studies (Sanchidrián et al., 2012). DEM-derived and empirically estimated block volumes show similar trends and comparable magnitudes in fragmentation behaviour, which is mainly controlled by blast design and rock mass characteristics, consistent with previous DEM and empirical investigations (Jing 2003; Jing and Hudson 2002). The validation of field measurements versus DEM methods: the DEM slightly overpredicts absolute volumes, but its level is higher than that of other methods; this behaviour is widely reported in previous research (Potyondy and Cundall, 2004). The close correlation among the measured, DEM, and empirical results verifies the reliability of the proposed framework and suggests the need for careful calibration and quality assurance procedures before adopting image-based fragmentation methods to get reliable results.

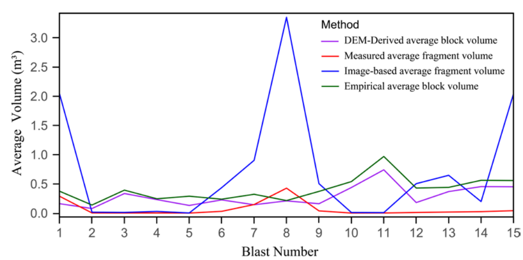

Figure 11: *Comparison between average in situ block volume and blast-induced fragment volume showing fragmentation trends obtained from different methods.*

Conclusion

An integrated approach of empirical, image-based and numerical methods based on DEM has quantified the pre-blast natural block geometry and blast-induced fragment morphology in the rock masses of the Himalayan terrain. The natural blocks exhibited cubical geometries governed by in situ joint spacing, discontinuity orientation and persistence. However, the blast-induced fragments were dominated by bladed and elongated shapes resulting from strong anisotropy and preferential splitting along structural planes, rather than along orthogonal block boundaries. The reliability of the adopted methodology was verified by statistical validation. The field-measured and image-based fragment volumes correlated well by a high coefficient of determination ($R^2 = 0.786$) and a low p-value ($p < 0.001$). Similarly, the empirical block volume estimation showed a strong relationship with the DEM-based block volumes ($R^2 = 0.831$, $p < 0.001$), with approximately 83% predictive performance. A comparative analysis of these methodologies reveals their strengths and limitations. The image-based analysis provides an efficient and practical approach to fragmentation estimates with minor variation introduced by two-dimensional effects such as occlusion, overlap, and scale uncertainty. In contrast, empirical and numerical approaches yield more reliable volume predictions by incorporating a three-dimensional structural analysis. This validated framework presents a practical solution for blast design optimisation, muck flow efficiency, and tunnelling performance in anisotropic jointed rock masses. Thus, these findings enhance the importance of integrating field measurements, image analysis, and numerical modelling to accomplish high-fidelity predictions of rock fragmentation and improve underground excavation processes in the geologically complex terrains of the Himalayas.

Acknowledgments

We would like to acknowledge Department of Geology, Tri-Chandra Multiple Campus and the anonymous reviewers.

Author's Contribution

NS: Conceptualization, methodology, data collection and interpretation, software (numerical modelling) and writing original draft. BT: Data collection and interpretation, methodology, numerical modelling, writing and editing. KKS: Data interpretation, writing, review and editing. PBT: Interpretation of results, review, editing and supervision.

Conflict of Interest

The authors declare no conflicts of interest.

References

Aliabadian, Z. and Sharafisafa, M. 2014, Distinct element modeling of the effect of joint persistence on dynamic fracturing of jointed rock masses. Applied Mechanics and Materials. 553: 445–451. https://doi.org/10.4028/www.scientific.net/AMM.553.445

Bronshtein, I. N., Semendyayev, K. A., Musiol, G., and Mühlig, H. 2015, *Handbook of Mathematics* (6th ed.), Springer.

Ghaedi G. M., Bahaaddini, M. and Amiri Hossaini, M. 2022, Estimation of in-situ block size distribution in jointed rock masses using combined photogrammetry and discrete fracture network. Journal of Mining and Environment, 13(1): 175–184.

Guo, Q., Wang, Y., Yang, S., and Xiang, Z.

2022, A method of blasted rock image segmentation based on improved watershed algorithm. Sci Rep., 12(1): 7143. doi: 10.1038/s41598-022-11351-0.

Jing, L. 2003, Review of techniques, advances and outstanding issues in numerical modelling for rock mechanics and rock engineering. International Journal of Rock Mechanics and Mining Sciences, 40(3): 283–353. https://doi.org/10.1016/S1365-1609(03)00013-3.

Jing, L. and Hudson, J.A. 2002, Numerical methods in rock mechanics, International Journal of Rock Mechanics and Mining Sciences, 39(4): 409–427. https://doi.org/10.1016/S1365-1609(02)00065-5.

Johansson, D. and Ouchterlony, F. 2013, Shock wave interactions in rock blasting: the use of short delays to improve fragmentation in model-scale. Rock Mechanics and Rock Engineering, 46(1): 1–18. https://doi.org/10.1007/s00603-012-0249-7.

Kinyua, E. M., Jianhua, Z., Kasomo, Mauti, R. M., D. and Mwangangi, J. 2022, A review of the influence of blast fragmentation on downstream processing of metal ores, Minerals Engineering, Vol. 186, 107743. https://doi.org/10.1016/j.mineng.2022.107743.

Koulibaly, A. S., Shahbazi, A., Saeidi, A., Rouleau, A., Quirion, M. and Chesnaux, R. 2023, Advancements in rock block volume calculation by analytical method for geological engineering applications. Environmental Earth Sciences, 82(13), 344.

Kujundžić, T., Klanfar, M., Korman, T. and Briševac, Z. 2021, Influence of Crushed Rock Properties on the Productivity of a Hydraulic Excavator. Applied Sciences. 11: 1–15. 10.3390/app11052345.

Maerz, N. H. and Zhou, W., 1999, Flat and elongated: Advances using digital image analysis. Center For Aggregates Research (ICAR) Seventh Annual Symposium Proceedings, Austin Texas, April 19-21, B1-4-1 to B1-4-12.

Maerz, N. H., Palangio, T. C. and Franklin, J. A. 1996, WipFrag Image Based Granulometry System. Proceedings of the FRAGBLAST 5 Workshop on Measurement of Blast Fragmentation (1996, Montreal, Quebec, Canada).

Ouchterlony, F. and Sanchidrián, J. A. 2019, A review of development of better prediction equations for blast fragmentation, Journal of Rock Mechanics and Geotechnical Engineering, 11(5): 1094–1109, https://doi.org/10.1016/j.jrmge.2019.03.001.

Palmström, A. 2005, Measurements of and correlations between block size and Rock Quality Designation (RQD). Tunnelling and Underground Space Technology, 20(4): 362–377. https://doi.org/10.1016/j.tust.2005.01.005.

Potyondy, D. O. and Cundall, P. A. 2004, A bonded-particle model for rock. International Journal of Rock Mechanics and Mining Sciences, 41(8): 1329–1364. https://doi.org/10.1016/j.ijrmms.2004.09.011.

Rahman, M. A., Shahrin, M. I., Abdullah, R. A., Sa'ari, R. 2025, Influence of Joint Orientation on Blast-Induced Fracture

Patterns in Granite Rock Using Discrete Element Method. Malaysian Journal of Civil Engineering, 37(2), 31–37. https://doi.org/10.11113/mjce.v37.23751.

Read, J. and Stacey, P. 2010, Guidelines for Open Pit Slope Design. SCIRO Publishing, Clayton. https://doi.org/10.1071/9780643101104.

Sanchidrián, J. A. and Ouchterlony, F. 2017, A distribution-free description of fragmentation by blasting based on dimensional analysis. Rock Mechanics and Rock Engineering, 50(4): 781–806. https://doi.org/10.1007/s00603-016-1131-9.

Sanchidrián, J. A. and Singh, A. K. 2012, Measurement and analysis of blast fragmentation. In the 10th International Symposium on Rock Fragmentation by Blasting, India, New Delhi, pp. 24–25.

Sanchidrián, J. A., Ouchterlony, F., Segarra, P. and Moser, P. 2014, Size distribution functions for rock fragments. International Journal of Rock Mechanics and Mining Sciences, Vol. 71: 381–394. https://doi.org/10.1016/j.ijrmms.2014.08.007.

Shrestha, N., Thapaliya, B. and Thapa, P. B. 2026, Evaluation of Empirical Approaches in Estimating the Deformation Modulus of Rock Masses in the Himalayan Region. Geotech. Geol. Eng. 44, 70. https://doi.org/10.1007/s10706-025-03592-3.

Shrestha, N., Thapaliya, B., and Ulak, P. D. 2023, Geological study along Sipaghat-Panchkhal-Sukute area, Kavreplanchowk and Sindhupalchowk districts, Lesser Himalaya, central Nepal. Journal of Nepal Geological Society, Vol. 65: 129–140. https://doi.org/10.3126/jngs.v65i01.57772.

Singh, P. K., Roy, M. P. Paswan, R. K., Sarim, M., Kumar, S. and Jha, R. R. 2016, Rock fragmentation control in opencast blasting. Journal of Rock Mechanics and Geotechnical Engineering, 8(2): 225–237, https://doi.org/10.1016/j.jrmge.2015.10.005.

Sneed, E. D. and Folk, R. L. 1958, Pebbles in the lower Colorado River, Texas: A study in particle morphogenesis. Journal of Geology, 66(2): 114–150. https://doi.org/10.1086/626490.

Song, F., Rodriguez-Dono, A. and Sanchez Farfan, P. 2022, Modelling underground excavations in rock masses with anisotropic time-dependent behaviour. Geomech. Geophys. Geo-energ. Geo-resour. 8, 146. https://doi.org/10.1007/s40948-022-00440-z.

Thapaliya, B., Shrestha, N., Acharya, M.S., Yadav, S. K. and Thapa P. B. 2025, Computational Optimization of Tunnel Support Systems Under Static and Dynamic Loads in the Himalayan Region. Geotech. Geol. Eng. 43, 302. https://doi.org/10.1007/s10706-025-03273-1.

Zeng, R., Ji, F., Li, Z., Wu, C. F., Lu, Y. P. and Ding, J. L. 2025, Size effect and parameter evaluation of jointed rock mass via discrete element method. Environmental Earth Sciences, 84(16), 462.

Zingg, T. 1935, Beitrag zur Schotteranalyse. Schweizerische Mineralogische und Petrographische Mitteilungen, 15: 39–140.